Bioactive Materials 13 (2022) 96–104

Contents lists available at ScienceDirect

Bioactive Materials

journal homepage: www.keaipublishing.com/en/journals/bioactive-materials

Ultrathin tellurium nanosheets for simultaneous cancer thermo-chemotherapy

Wen Pan [a,1], Chuang Liu [d,1], Yunhui Li [a,**], Yang Yang [a], Wenliang Li [c], Chan Feng [b,d,***], Leijiao Li [a,*]

[a] School of Chemistry and Environmental Engineering, Changchun University of Science and Technology, Changchun, 130022, China
[b] Department of Respiratory Medicine, Sir Run Run Shaw Hospital, Zhejiang University School of Medicine, Hangzhou, Zhejiang, 310016, China
[c] Jilin Collaborative Innovation Center for Antibody Engineering, Jilin Medical University, Jilin, 132013, China
[d] Center for Nanomedicine and Department of Anesthesiology, Brigham and Women's Hospital, Harvard Medical School, Boston, MA, 02115, United States

ARTICLE INFO

Keywords:
Two-dimensional materials
Tellurium
Photothermal therapy
Chemotherapy
Synergetic therapy

ABSTRACT

The emerging two-dimensional monoelemental materials (2D Xenes) have been commonly supposed as promising drug delivery carriers, photothermal and photodynamic therapeutic agents, biosensors, theranostics, and some other candidates for biomedical applications. Here, high-performance and bioactive ultrathin 2D Tellurium nanosheets (Te NSs) are prepared by a simple but efficient liquid-phase exfoliation approach. The as-obtained Te NSs possess a mean size of ~90 nm and a mean thickness of ~5.43 nm. The pegylation Te NSs (Te-PEG NSs) possess excellent biocompatibility and stability. The Te-PEG NSs could generate local hyperthermia with a remarkable photothermal conversion efficiency of about 55% under 808 nm laser irradiation. Additionally, Te-PEG NSs exhibit an extremely high loading capacity of chemo drug (~162%) owing to their ultra-high surface area and tumor microenvironment-triggered drug release superiority. The results of *in vivo* experiments show that the Te-PEG NSs have higher tumor elimination efficiency via the combination of photothermal and chemotherapy, comparing to any other single therapeutic modalities. Therefore, our work not only highlights the promising potentials of tellurene as an ideal anti-cancer platform but also expands the application of 2D Te for cancer nanomedicine.

1. Introduction

Since Geim and co-workers reported the stripping of graphene in 2004, the exploration of two-dimensional (2D) nanoarchitectures has been pushed to a climax [1]. In recent decades, the frontiers of 2D materials beyond graphene keep emerging and innovating [2]. Prominent examples include graphitic carbon nitride (g-C_3N_4) [3], 2D covalent-organic frameworks (COFs) [4], 2D metal-organic frameworks (MOFs) [5], 2D transition metal dichalcogenides (TMDs) [6], hexagonal boron nitride (h-BN) [7], layered double hydroxides (LDH) [8], 2D clay materials [9] and monoelemental materials (Xenes) [10]. These emerging functional materials could achieve various applications due to their excellent properties, such as optoelectronics, biomedicine, solar cells, high-efficiency catalysts, *etc.* [11] Among the family of 2D nanomaterials, Xenes are one type of novel member, which possess excellent biocompatibility and advantageous applications in the biomedical field [12]. Owing to the remarkable photonic, physical, and chemical properties of Xenes, they have been regarded as ideal candidates in diagnosis and optical therapeutic systems, such as photoacoustic imaging (PAI) [13], X-ray computed tomography (CT) [14], photoluminescence lifetime imaging (PLTI) [15], fluorescence imaging (FI) [16], photosensitizers (PSs) [17] and photothermal agents (PTAs) [18].

Among Xenes, tellurium (Te) is an essential raw material for semiconductor manufacturing because of its excellent optoelectronic

Peer review under responsibility of KeAi Communications Co., Ltd.
* Corresponding author.
** Corresponding author.
*** Corresponding author. Department of Respiratory Medicine, Sir Run Run Shaw Hospital, Zhejiang University School of Medicine, Hangzhou, Zhejiang, 310016, China.
E-mail addresses: liyh@cust.edu.cn (Y. Li), chanfeng_zju@163.com (C. Feng), lileijiao@cust.edu.cn (L. Li).
[1] These authors contributed equally to this work.

https://doi.org/10.1016/j.bioactmat.2021.11.010
Received 12 August 2021; Received in revised form 5 October 2021; Accepted 5 November 2021
Available online 17 November 2021

characters. Te-based materials and their applications in the aspect of electrochemistry and optoelectronics have been widely studied [19]. Recently, the potential of Te-based nanomaterials was revealed in biomedical applications. For instance, Te nanodots and Te nanorods were reported for generating active electrons/holes under nearinfrared (NIR) irradiation to acquire high-efficiency photothermal transformation and to react with the ambient environment for inducing oxidative stress. Thus, Te-based nanomaterials were supposed to be an excellent platform for photo-induced synergistic anti-cancer therapy [20]. Te nanoneedles possess both high photothermal conversion efficiency and NIR laser-enhanced antioxidative activity toward scavenging free radicals [21a]. Te nanostars could achieve RT-enhanced anti-PD-1 checkpoint blockade immunotherapy [21b]. Besides, the low cytotoxicity of Te-based nanostructures in different cells was preliminarily certified, suggesting their excellent biocompatibility.

However, the efficient manufacture and biomedical applications of Te are still needed to be further investigated. For instance, Te has anisotropic characteristics with chain-like architecture, which is much similar in chemical, physical properties of black phosphorus (BP) [2a,9c, 14,17]. Likewise, there is covalently bonded between adjacent Te atoms, while weak van der Waals' interaction existed between adjacent chains. Aqueous exfoliation is acknowledged as a practical and straightforward strategy to obtain 2D nanomaterials by breaking down the weak interlayer interactions [22]. Notably, Te nanosheets (Te NSs) with a few layers or even a monolayer have better optical-response properties and fascinating electronic characters. Moreover, the extraordinary surface area and facile surface functionalization are more conducive for nanosheets to load drugs [10a,13,18]. Therefore, 2D lamellar Te NSs could be a better choice for serving both as a drug delivery platform and photothermal agents.

Herein, we presented a 2D ultrathin Te NSs-based thermo-chemotherapeutic anti-tumor platform with excellent biocompatibility (Scheme 1). The ultrathin Te NSs were obtained by the liquid phase stripping technique and then surface-modified with PEG. The Te-PEG NSs exhibit encouraging loading capacity of chemo drugs as well as remarkable photothermal conversion efficiency. The scheme showed the hyperthermia effect and controlled release upon laser irradiation for synergistic cancer treatment. This work highlights the promising potentials of Te-PEG NSs as an ideal nanoplatform for simultaneous cancer thermo-chemotherapy.

2. Materials and methods

2.1. Materials

Tellurium bulks (Te, 99.99%) and isopropyl alcohol (IPA, HPLC) were purchased from Sigma-Aldrich (Saint Louis, Missouri, USA). 1,2-distearoyl-sn-glycero-3-phosphoethanolamine-N-[methoxy(polyethyleneglycol)] (DSPE-PEG) was purchased from Hangzhou Xinqiao Biological Technology Co., Ltd. (Hangzhou, China). Doxorubicin (DOX) was obtained from Hubei Kangming de Pharmaceutical Chemical Co., Ltd. (Hubei, China). These chemicals are used as received.

2.2. Synthesis of Te NSs

Briefly, the Te NSs were prepared from the Te bulk by the liquid phase stripping technique. 0.1 g of bulk Te was put into an agate mortar for 30 min to form a fine powder, then transferred into a 50 mL centrifuge tube. 20 mL of IPA was added into the above centrifuge tube to obtain a muddy suspension solution. Liquid-phase exfoliation was performed in ice water for 8 h by an ultrasonic probe (Amplifier: 52%, On/Off cycle: 4 s/2 s). The low-temperature condition (less than 5 °C) of the system could reduce the oxidation during the exfoliation procedure. The obtained brown-black dispersion was centrifuged at 6000×*g* for 30 min. The unexfoliated bulk Te was abandoned as sediment, meanwhile, the supernatant containing Te NSs was carefully collected. The prepared

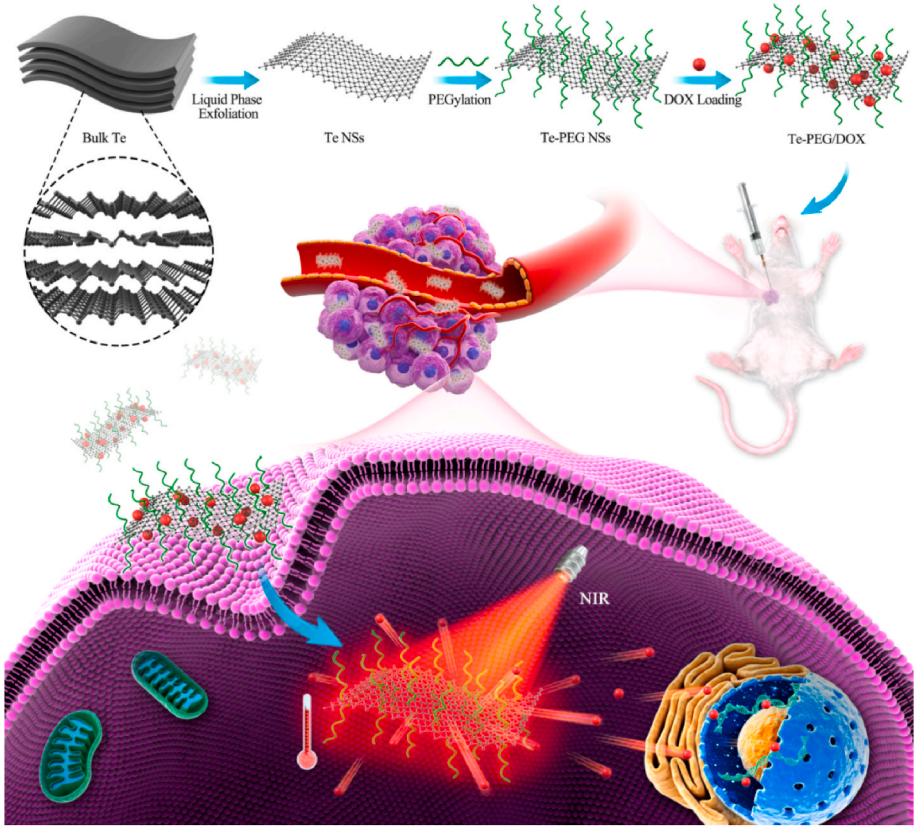

Scheme 1. Schematically illustration of the preparation process and multi-modal cancer therapy of Te-PEG/DOX NSs.

2D Te NSs were dried in a vacuum oven at room temperature.

2.3. PEG coating on the surface of Te NSs

A simple and fast method was applied for the surface modification of Te NSs to prepare Te-PEG NSs. In particular, 0.05 g Te and 0.5 g DSPE-PEG were added to 100 mL of chloroform and sonicated for 20 min. Then the mixed solution was evaporated to remove chloroform. The obtained solid matter was dissolved in an ultrapure aqueous solution and performed dialysis within 24 h to remove the excess DSPE-PEG. After 48 h, the sample was stored under 4 °C.

2.4. Construction of a nano drug-loading system

Different masses of DOX (0.5, 1.5, 2.5, 3.5, 4.5, 5.5 mg) were added to PBS solution of Te-PEG with a concentration of 500 μg mL^{-1} (raw material ratio DOX/NSs = 1, 3, 5, 7, 9, 11). After being agitated overnight at room temperature, DOX was loaded on the surface of Te-PEG by coulombic forces. And then, the supererogatory DOX was removed by washing several times use ultrapure water.

2.5. Drug loading and release

Since DOX has a unique spectral absorption at 490 nm, we firstly investigated the spectral absorption of different concentrations of DOX aqueous solution. We plotted the standard curve based on the absorption intensity at 490 nm. Subsequently, the spectral absorption of Te-PEG and Te-PEG/DOX NSs was investigated separately. The concentration of DOX in the drug-loaded system was obtained by subtracting the intensity of the absorption peak of Te-PEG/DOX NSs from the peak intensity of Te-PEG, and the loading rate of Te NSs to DOX was calculated. 1 mL of Te-PEG/DOX NSs was placed in a dialysis bag and immersed in a 19 mL PBS solution with pH 7.4 as well as pH 5.0 and then shaken at 37 °C. 1 mL of solution was removed at a certain time point, and 1 mL of fresh PBS solution was replenished in time. The concentration of the external DOX solution was evaluated by examining the ultraviolet absorption spectrum, and the release rate of DOX by Te-PEG/DOX was calculated. The photothermal induced release of DOX performance test was performed under the same condition with an additional 808 near-infrared light at 2 Wcm^{-2} for 10 min at each specific time.

2.6. The photothermal properties of Te-PEG

The temperature changes of Te-PEG solution were recorded by the photothermal imager at different concentrations (0–200 μg mL^{-1}) at different power densities (2–4 W cm^{-2}) with 808 nm near-infrared laser irradiation for 10 min. The photo-thermal conversion efficiency of Te NSs was estimated according to the previous literature. An 808 nm laser with 2 W cm^{-2} was performed to irradiate 1 mL of Te-PEG NSs (200 μg mL^{-1}) and a photothermal imager monitored the solution temperature for 10 min, then turned off the laser and monitored the solution temperature for 10 min. The calculations of photothermal conversion efficiency were detailed in the Supporting Information. First-principles calculations within the generalized gradient approximation (GGA) were carried out by the Vienna ab initio simulation package (VASP) [23]. The method of the calculations can be found in the Supporting Information.

2.7. Cell culture

Mouse breast cancer cell 4T1, human breast cancer cell MCF-7, human cervical cancer cell HeLa and mouse fibroblast cell L929 were cultured in DMEM high glucose medium containing 10% fetal bovine serum and 10% penicillin/streptomycin. Mouse colon cancer cell line CT26 was cultured in RPMI-1640 medium containing 10% fetal bovine serum and 10% penicillin/streptomycin.

2.8. Cytotoxicity test

The MTT assay confirmed the cytotoxicity of the materials. 4T1 cells and L929 cells were respectively inoculated in the 96-well cell culture plate with the inoculation density of 6000 cells/well, and cultured overnight at 37 °C to make it stick wall deformation. The cells were cultured for 12 h to cause their adherent deformation. Different concentrations of Te-PEG NSs (800, 400, 200, 100, 50, 25, 12.5 μg mL^{-1}) were added then, 5 sets of duplicate wells were allocated for each concentration, and PBS control group was allocated at the same time. After culturing for 24 h in a 37 °C incubator, the drug solution was washed several times with PBS. Refill 150 μL of DMSO solution per well. After shaking for a couple of minutes, the absorbance of each well at 490 nm was determined through a microplate reader. The calculations of Cell viability can be found in the Supporting Information.

2.9. Cell endocytosis experiment

Incubate 4T1 cells with Te-PEG/DOX NSs (25 μg mL^{-1}) in the cell incubator for different times (10 min, 1 h, 2 h, 4 h), and set 0 min as the control group. The cells were then washed with PBS several times, whereafter fixed with 4% paraformaldehyde for 15 min, therewith stained with DAPI for another 15 min. The cell endocytosis was observed under a light microscope.

2.10. In vitro tumor inhibition experiment

Using 4T1 cells as the cell source, the photothermal effect of Te-PEG NSs (Te concentrations were 200, 150, 100, 50, 25, 0 μg mL^{-1}), chemotherapy effect of Te-PEG/DOX NSs (DOX concentrations were 200, 100, 50, 25, 12, 6, 3, 1.5 μg mL^{-1}) and the synergistic treatment (Te-PEG NSs, Te-PEG NSs + NIR, Te-PEG/DOX NSs, Te-PEG/DOX NSs + NIR) were investigated by MTT test. Apoptosis staining was performed using the Annexin V-FITC/PI double-stained apoptosis detection kit. The experimental groups were: Te-PEG NSs group, Te-PEG NSs + NIR group, Te-PEG/DOX NSs group, Te-PEG/DOX NSs + NIR group (Te concentration were 50 μg mL^{-1}), monitored by flow cytometry. All photothermal treatments were inspired by an 808 nm near-infrared light for 10 min at 2 W cm^{-2}.

2.11. Tumor model

Six-week-old female BALB/c mice were purchased from the Center for Experimental Animals of Jilin University and raised in SPF animal rooms. All animal experiments, including animal care, dosing, and termination, were performed according to the guidelines of the local Animal Ethics Committee of Changchun University of Science and Technology. Animal testing and research conform to all relevant ethical regulations. All institutional and national guidelines for the care and use of laboratory animals were followed. About 100 μL of 4T1 cells in the DMEM medium were subcutaneously implanted into the armpit of the tumor-bearing BALB/c mice with a dose of 2×10^6 cells. The volume of the tumor was acquired by a vernier caliper, and a tumor inhibition test was performed when the tumor grew to 70–100 mm^3.

2.12. In vivo thermal imaging

The injection was performed on the tumor-bearing BALB/c mice at tumor subcutaneous with 250 μL PBS or Te-PEG (500 μg/mL) solution[12]. After 3 h of injection, the anesthetized mice were tranquilized with pentobarbital at the dose of 6 mg/kg by intraperitoneal injection. Subsequently, the tumor site of the mouse was exposed to an 808 nm laser for 10 min at 2 Wcm^{-2}. The whole-body temperature of the mice was under constant surveillance by a near-infrared imager (Fluke TiS40) during the entire laser irradiation process.

2.13. In vivo tumor inhibition experiment

The tumor-bearing BALB/c mice were randomly grouped into seven subsets (n = 4 in each subset), including (1) PBS, (2) PBS + NIR group, (3) Te-PEG group (4) Te-PEG + NIR group, (5) DOX, (6) Te-PEG/DOX group, (7) Te-PEG/DOX + NIR group. 250 μL solution of the corresponding sample (500 μg/mL) was injected at tumor subcutaneous[12]. After 3 h, all NIR groups were exposed under an 808 nm near-infrared light at the tumor site for 10 min. The mice were monitored and weighed daily for two weeks. The laboratory-bred mice were sacrificed and the major organs samples were collected ultimately. All the animal experiments are conducted following experimental animal ethics. Statistical analysis was performed by student's test. The statistical significance different was indicated *$p < 0.05$, **$p < 0.01$, ***$p < 0.001$.

3. Results and discussion

3.1. Characterization of Te NSs

The Te NSs were detached from their bulk materials via a simple liquid-phase exfoliation in isopropyl alcohol (IPA) solution (Fig. 1a). As shown in Fig. 1b, X-ray diffractometry (XRD) spectra of Te NSs was consistent with the standard card PDF#86-2268. There was a remarkable diffraction peak at 27.5° corresponding to (011) crystal plane of element Te, matching well with the references. [19c] Besides, the good purity of the prepared Te NSs was illustrated through X-ray photoelectron spectroscopy (XPS) as well (Fig. 1c). Apart from the C 1s and O 1s peaks, only two pretty strong peaks were detected at 573.5 eV and 538.5 eV corresponding to $3d_{5/2}$ and $3d_{3/2}$ orbitals of Te^0. Hence, the purity of the final product was repeatedly proven according to the above experiments.

The morphology, size, and thickness of the Te NSs was determined by transmission electron microscopy (TEM) and atomic force microscopy (AFM), respectively. As shown in Fig. 1d, the transverse dimension of Te NSs is about 90 nm. In addition, according to the high-resolution TEM result, Te NSs possessed a high degree of crystallinity with the unambiguous lattice fringes of 0.33 nm, which was consistent with the previous study [16]. The AFM images indicated the successful preparation of 2D ultrathin Te NSs with a thickness of about 5.43 nm (Fig. 1e). As a consequence, the liquid-phase exfoliation strategy was proved to be effective for the preparation of 2D monoelemental Te NSs.

3.2. Dispersibility and stability of Te NSs and Te-PEG NSs

Considering that PEGylation is one of the most common strategies to improve the *in vivo* stability and biocompatibility of Xenes [10b,13], DSPE-PEG was selected as a modification on Te NSs via van der Waals forces (Te-PEG NSs). More broadly, the Zeta potential of PEGylation Te NSs was increased compared with that of frugal Te NSs, further indicating that the surface modification springs from the electrostatic interaction between DSPE-PEG and Te NSs (Fig. S1, Supporting Information). Moreover, we found that there was no visible precipitation when PEG-Te NSs dispersed in an aqueous solution for 24 h, suggesting the good stability and dispersibility of PEG-Te NSs (Fig. S2a, Supporting Information).

To further compare the stability of Te NSs and Te-PEG NSs, we observed their dispersibility in different solvent systems for seven days, such as water, phosphate-buffered saline, and cell high-glucose DMEM. We also evaluated the size change of Te NSs and Te-PEG NSs in different solvent systems via dynamic light scattering (DLS) shown in Figs. S2b–g. The unadorned Te NSs were precipitated off gradually in the above kinds of solvent as time proceeds. At the same time, the negligible sediment could be observed visually even in PBS or DMEM solution of Te-PEG NSs. These results suggested that Te NSs would aggregate rapidly

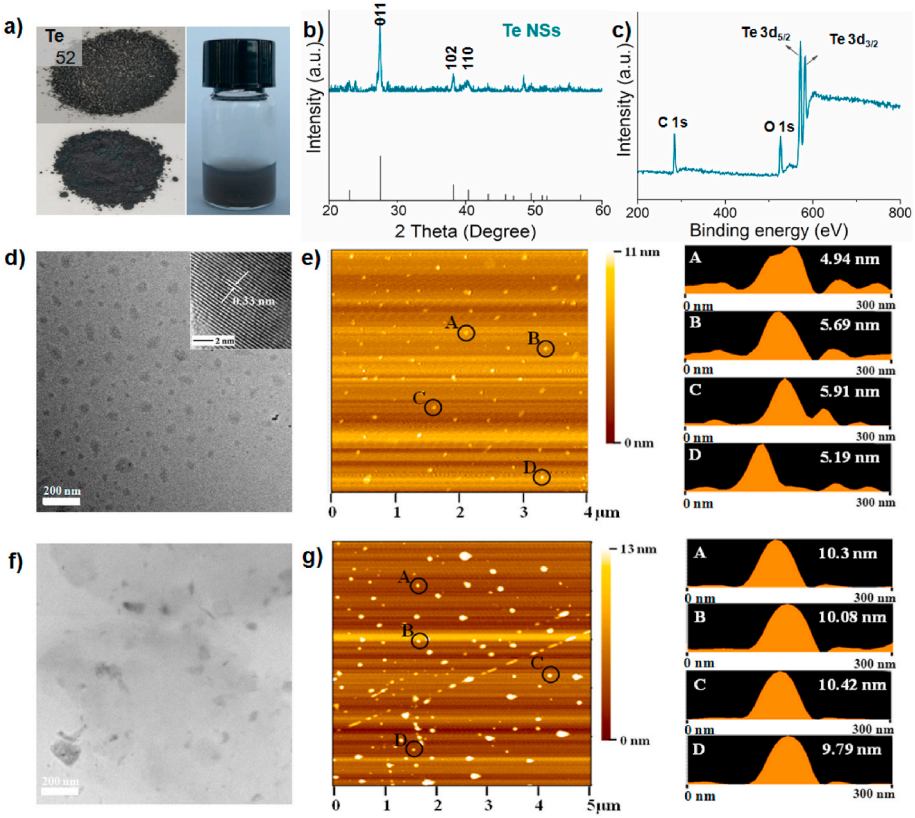

Fig. 1. Preparation and characterization of ultrathin 2D Te and Te-PEG NSs. a) photos of bulk tellurium, tellurium powder, and Te NSs solution during the preparation process. b) XRD pattern and c) XPS pattern of Te NSs.TEM images and AFM images of Te NSs (d, e) and Te-PEG NSs (f, g).

without PEGylation. The size distribution of Te-PEG NSs maintained unaltered with the size of about 100 nm throughout monitored with dynamic light scattering (DLS), also indicating the improved long-term stability and dispersity via PEGylation. Therefore, the prepared Te-PEG NSs exhibited quite excellent stability and dispersity in different physiological conditions, which was a prerequisite for the following biomedical application. Compared with naked Te NSs, the Te-PEG NSs remained in a sheet-like morphology with a slight size shrinkage (~80 nm) (Fig. 1f), which may be ascribed to the further ultrasonic treatment during the PEGylation process [24]. Te-PEG NSs with a thickness of about 10.15 nm were a little thicker than that of Te NSs (5.43 nm) (Fig. 1g), which also proved that DSPE-PEG was successfully modified to the surface of Te NSs.

3.3. Photothermal conversion efficiency of Te-PEG NSs

Ultraviolet–visible (UV–vis)-NIR absorbance spectra indicated Te-PEG NSs showed a wide and strong absorption within the scope from UV to NIR (Fig. 2a). The density of states (DOS) of the dual-layered Te (011) was calculated to clarify the electronic behavior in Te NSs (Fig. 2b). The conduction band (CB) minimum and the valence band (VB) maximum were mostly comprised of Te 5p along with a spot of Te 5s. Te NSs exhibits a quasi-zero-band gap character resulting in fantastic electronic transport properties, which is the probable reason for its photothermal conversion ability [25]. Encouraged by the promising NIR absorption ability of Te-PEG NSs, the *in vitro* photothermal conversion properties of Te-PEG NSs were evaluated by an infrared camera. As illustrated in Fig. 2c, upon an 808 nm laser irradiation (2 W cm^{-2}) for 10 min, the highest temperature increase (ΔT_{max}) of Te-PEG NSs solutions was 15.3 °C. Moreover, higher ΔT_{max} could be obtained with the increase of light intensity at the same Te-PEG NSs concentration (Fig. S3, Supporting Information). Then, according to the reported calculational method as shown in Fig. S4 [26], the photothermal conversion efficiency of Te-PEG NSs reached 55%, which was superior to that of numerous conventional 2D PTAs including graphene oxide (25%) [27], molybdenum disulfide (MoS_2) nanoflakes (27.6%) [28] and black phosphorus (BP) nanosheets (29.8%) [18]. Moreover, it was even higher than other forms of Te-based nanomaterials, such as Te nanorods (37.4%) [20b], Te nanodots (40%) [20a], and Te nanoneedles (43.9%) [21].

3.4. Photostability of Te-PEG NSs

Excellent photostability is also a significant element and plays a crucial role in PTT. Consequently, the photostability of Te-PEG NSs was investigated via a series of experiments. As presented in Fig. 2d, the photothermal effect of each heating and cooling cycle was similar to that of the first time, suggesting the excellent optical stability of Te-PEG NSs. UV–Vis absorption spectrum of Te-PEG NSs before and after four times of light irradiation was almost constant (Fig. 2e). Accordingly, Te-PEG NSs could easily accomplish the conversion of near-infrared light to thermal energy and then rapidly trigger the rise of the ambient temperature to achieve an effective and recyclable PTT.

3.5. Te-PEG NSs for anti-tumor thermo-chemotherapy

Many 2D nanomaterials were widely reported as theranostic delivery platforms [29]. Owing to the large specific surface area, the prepared Te-PEG NSs were also supposed to be a drug delivery platform with the function of simultaneous thermo-chemotherapy. Doxorubicin (DOX), a broad-spectrum chemotherapeutic drug in clinical, was chosen as a modal anti-tumor drug, which was loaded on Te-PEG NSs via strong π-π stacking interaction. The DOX-loaded Te-PEG NSs (Te-PEG/DOX NSs) were obtained by mixing Te-PEG NSs PBS solution with DOX at different feeding ratios. After removing excess free DOX, the DOX-loading rates of Te-PEG/DOX NSs at different feeding ratios (DOX: NSs) were shown in Fig. S5. The loading capacity of DOX increased in a DOX/NSs feeding ratio-dependent manner, and the drug loading became saturation at a DOX/NSs feeding ratio of 7:1. The highest drug loading rate of PEG-Te

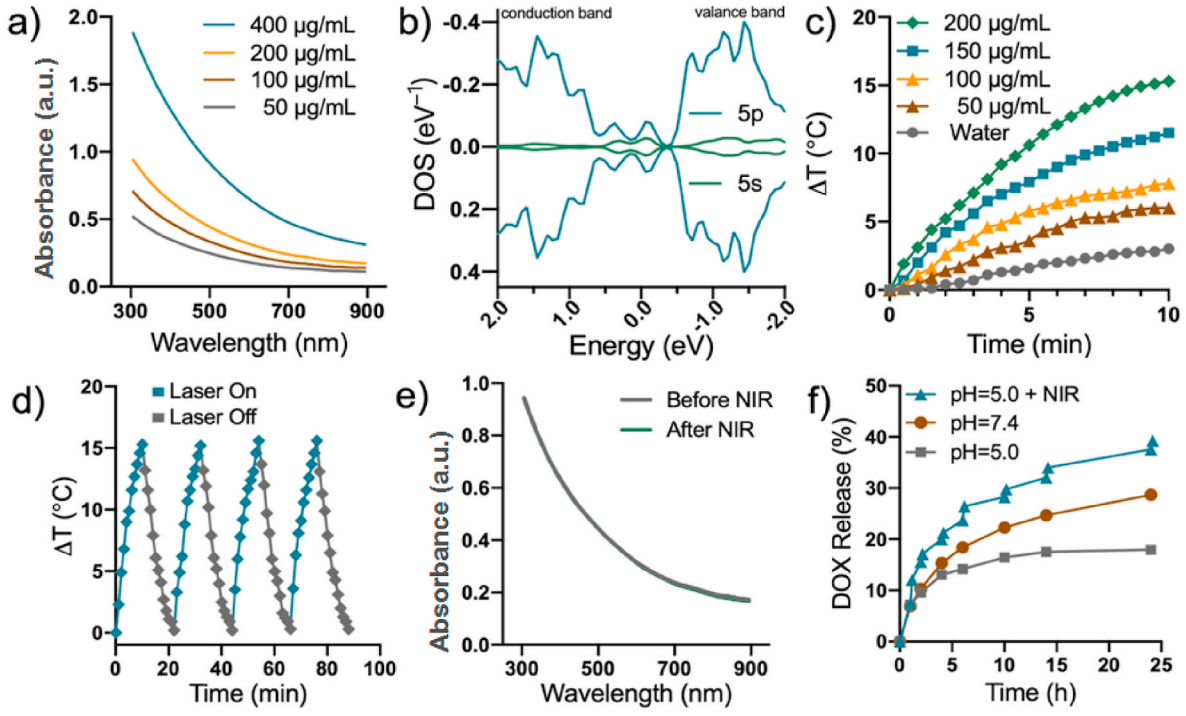

Fig. 2. Characterization of Te-PEG NSs for photonic drug delivery platform. a) Absorbance spectra of Te-PEG NSs dispersed in water at different concentrations. b) Density of states (DOS) of TeNSs. c) Temperature change and temperature elevation of the Te-PEG NSs with an 808 nm NIR laser (2 W cm^{-2}). d) Temperature elevation of the Te-PEG NSs for four laser on/off cycles with an 808 nm NIR laser (2 W cm^{-2}) in water. e) Absorbance spectra of Te-PEG NSs in water before and after four laser on/off cycles. f) Drug release kinetics of Te-PEG/DOX NSs at pH = 7.4 and pH = 5.0 (in the absence or presence of 2 W cm^{-2} NIR laser).

NSs was 162%, which was significantly superior to many previously reported nano-deliveries [18,30]. Te-PEG/DOX NSs at the feeding ratio of 7:1 (DOX: Te NSs) were chosen to use in the following experiments. Besides, the less negative charge of the Te-PEG/DOX NSs was plotted in Fig. S1) after DOX loading, indicating the successful DOX loading.

To investigate the low-pH triggered drug release, we observed DOX release behavior of Te-PEG/DOX NSs in pH 5.0 (the endosomal pH of cancer cells) and pH 7.4 (the physiological pH) PBS solutions at 37 °C for 24 h severally. As demonstrated in Fig. 2f, the *in vitro* drug release rate of DOX was about 18% at pH 7.0, whereas it was over 29% at pH 5.0. The pH-responsive *in vitro* drug release rate of Te-PEG/DOX NSs was similar to other 2D nanocarriers reported previously [17]. Furthermore, the irradiation triggered drug release was also studied. The DOX release rate under 808 nm irradiation increased abruptly as high as 39%, suggesting laser-induced local high temperature could accelerate DOX releasing from Te-PEG NSs [30]. Briefly, the faintly acid environment (pH = 5.0) and laser triggered DOX release of Te-PEG/DOX NSs would be advantages to achieve precise, controlled drug release in drug delivery for cancer therapy. Therefore, Te-PEG/DOX NSs were supposed to be an excellent drug delivery platform for anti-tumorthermo-chemotherapy.

3.6. *In vitro* safety and photothermal performance of Te-PEG/DOX NSs

Several different cell lines, including normal cells (L929 fibroblast cells) and cancer cells (4T1, CT26, MCF-7, and HeLa cell lines), were used to estimate the cytotoxicity of Te-PEG NSs *in vitro* (Fig. 3a). Te-PEG NSs solutions in different concentrations were co-incubated with the above-mentioned cell lines for 24 h. While the concentrations were gradually increased from 12 to 200 μg mL^{-1}, the cell viability rate remained steady at around 90%. At the low concentration, Te-PEG NSs exhibited a similar feature to various other Te-based nanostructures including Te NSs@GSH, Te nanoneedles, and Te nanorods. For instance, at the concentration of 25 μg mL^{-1}, the cell viability rate was above 90% (normal or tumor cells) after incubated with Te-PEG NSs for 24 h. Similarly, about 90% of HeLa cells survived after incubated with Te NSs@GSH, and it was about 80% MCF-7 cells after incubated with Te nanoneedles [17,21a]. In marked contrast, at the high concentration, the cell viability of neither normal nor tumor cells was affected after incubated with Te-PEG NSs, indicating that Te-PEG NSs possessed more superior biocompatibility than other Te-based nanomaterials [31]. The cell viability rate was only about 50% at 100 μg mL^{-1} of Te nanorods. Nevertheless, it was an approximate rate of 90% after incubated with Te-PEG NSs at the same concentration [32]. Importantly, even the Te-PEG NSs with a concentration (200 μg mL^{-1}) still showed no appreciable cytotoxicity, while the survival rate of both normal cell and cancer cell lines was above 90%. These outcomes suggested the excellent biocompatibility of Te-PEG NSs.

To investigate the *in vitro* photothermal performance of Te-PEG NSs, cell line 4T1 was selected as a model cancer cell in studies. 4T1 cells were treated by Te-PEG NSs and laser irradiation (Te-PEG NSs + laser). The cell survival rate decreased in a manner of Te-PEG NSs concentration-dependent under laser irradiation. As shown in Fig. 3b, approximately 90% of the 4T1 cells were killed by 200 μg mL^{-1} Te-PEG NSs-mediated hyperthermia, suggesting an excellent photothermal therapeutic effect. To further evaluate *in vitro* thermo-chemotherapy efficacy, 4T1 cell lines were respectively treated with Te-PEG NSs and

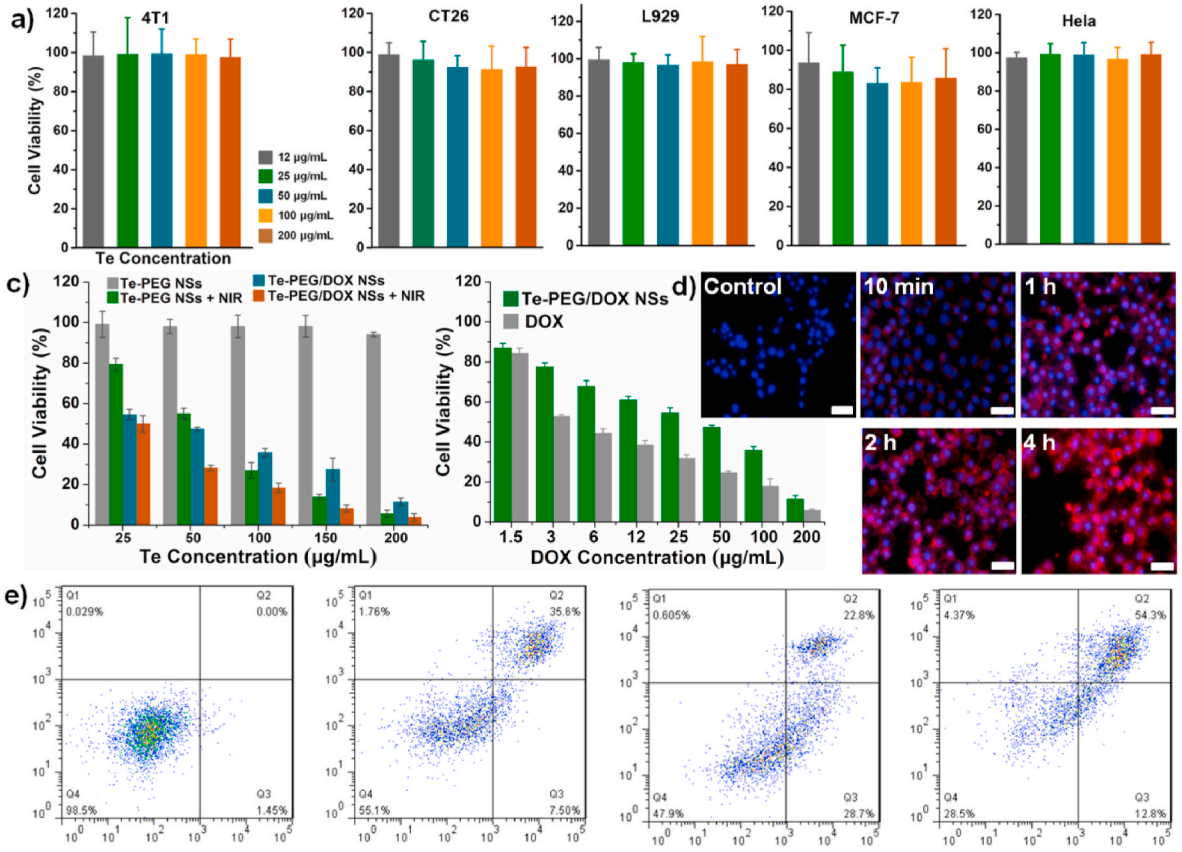

Fig. 3. Cell experiments. a) Relative viabilities of different cells after incubation with various concentrations of Te-PEG NSs for 24 h. b) Relative viabilities of 4T1 cells after various treatments at different Te NSs concentrations. c) Relative viabilities of 4T1 cells after 24 h incubation with free DOX and Te-PEG/DOX NSs at various concentrations. d) Cellular uptake of Te-PEG/DOX NSs by 4T1 cells at the dose of 25 μg mL^{-1} DOX after different incubation times, the cells are co-stained with Calcein-AM (green, live cells) and propidium iodide (red, dead cells). Scale bars represent 50 μm. e) The flow cytometry results revealing the various apoptosis levels of 4T1 cells under different treatments. (For interpretation of the references to colour in this figure legend, the reader is referred to the Web version of this article.)

Te-PEG/DOX NSs. After 4 h incubation, half of the treated cells in the above groups were exposed to laser irradiation (808 nm at 2 W cm^{-2}) for 10 min, while the other half of the cells were without laser exposure. The lowest cell viability in Te-PEG/DOX NSs with irradiation group was observed, suggesting significant thermo-chemotherapy efficacy. Especially when Te concentration was 200 μg mL^{-1}, most of the cells (96%) were dead in Te-PEG/DOX NSs with irradiation group. By contrast, other groups with thermotherapy efficacy or chemotherapy efficacy alone exhibited a lower cell death rate at the same Te concentration. Besides, the Te-PEG NSs without NIR irradiation didn't exhibit toxicity to 4T1 cells at tested concentrations, suggesting excellent biocompatibility of Te NSs. To investigate the synergistic thermo-chemotherapy effect of Te-PEG/DOX NSs, we tested cell viability of 4T1 cells treated by Te-PEG/DOX NSs without NIR laser irradiation, while cells treated by free DOX as control (Fig. 3c). It was found that the cell viability in Te-PEG/DOX NSs and free DOX groups decreased in DOX concentrations manner. In contrast, the cells treated by free DOX exhibited slightly lower cell viability than those in Te-PEG/DOX NSs group, owing to the faster cell internalization of small molecular DOX than Te-PEG/DOX NSs [33].

Subsequently, the cellular uptake of the synergistic thermo-chemotherapy platform Te-PEG/DOX NSs was also studied. As the confocal laser scanning microscopy (CLSM) photographs were shown in Fig. 3d, only a handful of Te-PEG/DOX NSs was taken up by 4T1 cells in the first 10 min. After 1 h incubation, a glow Te-PEG/DOX NSs increased gradually near the nucleus. When the incubation time extended to 4 h, the significant enhancement of DOX fluorescence accumulated both in the cytoplasm and nucleus, owing to a large amount of Te-PEG/DOX NSs uptaken. It indicated that the Te-PEG NSs based drug delivery platform could achieve effective cell internalization and deliver DOX to the nucleus exert an anti-cancer effect. Flow cytometry (FCM) results further confirmed the *in vitro* anticancer effects. As same as the results of cytotoxicity experiments, the highest cancer cell apoptosis rate was observed in thermo-chemotherapy of Te-PEG/DOX NSs (Fig. 3e). All these results confirmed Te-PEG/DOX NSs based thermo-chemotherapy could provide an excellent anti-cancer effect on a cellular level.

3.7. *In vivo* anti-cancer effect of Te-PEG/DOX NSs

We further investigate the *in vivo* anti-cancer effect of Te-PEG/DOX NSs on 4T1 tumor-bearing mice. The photothermal effect of Te-PEG NSs was evaluated by an infrared thermal imaging camera firstly. The temperature of the tumor rose steeply to 48.9 °C in Te-PEG NSs-treated mice, owing to the glorious photothermal conversion efficiency (Fig. 4a and b). In contrast, there was only a slight tumor temperature rise in saline-treated mice (ΔT = ~4.7 °C). Inspired by the excellent *in vivo* treatment effects, we further evaluated the combination therapy performance of PEG/DOX NSs. To be specific, tumor-bearing mice were segmented into seven groups with different treatments: 1) control group (saline); 2) saline + 808 nm laser; 3) Te-PEG NSs; 4) Te-PEG NSs + 808 nm laser; 5) DOX; 6) Te-PEG/DOX NSs; 7) PEG/DOX NSs + 808 nm laser. After 4 h intra-tumoral post-injection of saline, Te-PEG NSs, or Te-PEG/DOX NSs, the tumor sites were irradiated by 808 nm near-infrared light for 10 min or not. After different treatments, the volume and bodyweight of tumors in each group were estimated every couple of days during the two-week treatment.

As shown in Fig. 4c and e, Te-PEG/DOX NSs with NIR irradiation show a better therapeutic effect in the inhibition of tumor growth than other formulations. Besides, Te-PEG NSs under the NIR irradiation also exhibited better anti-tumor effect to some degree, compared with the other groups. On the contrary, the most rapid increase of tumor volume in the saline-treated group and saline + NIR-treated group, suggesting NIR irradiation had no significant anti-tumor effect. All the above results support the promoting effect of Te NSs drug delivery platform in anti-tumor treatment. Satisfactorily, the lowest tumor growth rate occurred in PEG/DOX NSs +808 nm-treated group before the observing endpoint.

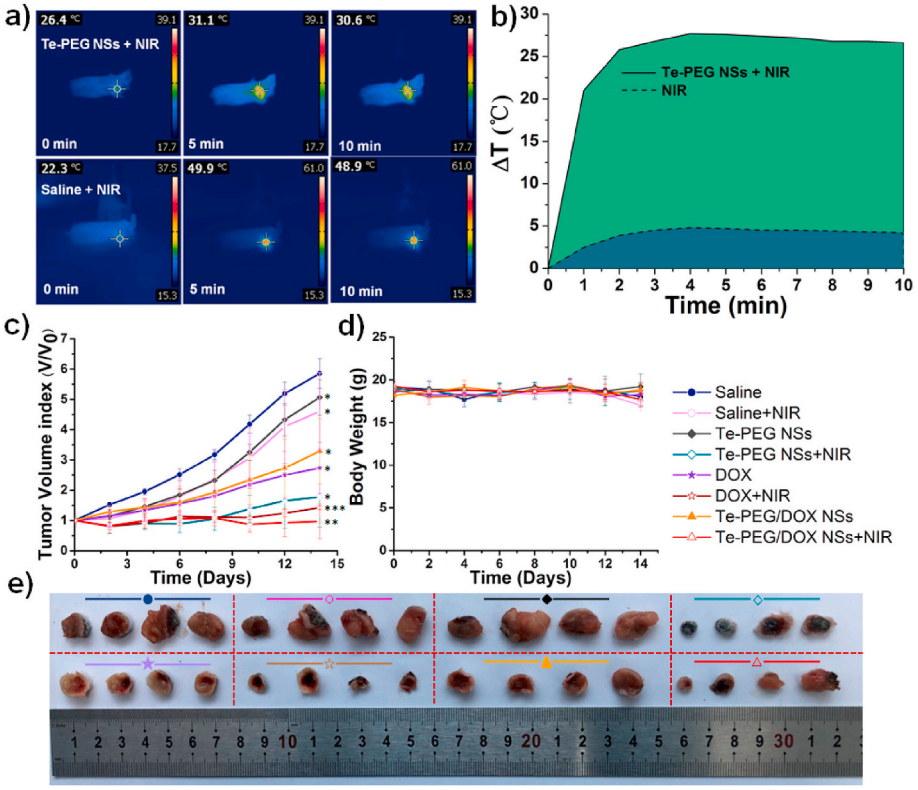

Fig. 4. *In vivo* imaging, biodistribution, and combined cancer therapy effect of Te-based NSs. a) *In vivo* NIR imaging and b) temperature elevation of tumor-bearing mice treated with 808 nm laser (2 W cm^{-2}) for 10 min. c) The relative tumor volume after different treatments. *p < 0.05, **p < 0.01, ***p < 0.001. d) The bodyweight of mice after different treatments. e) Tumor images of mice in different treatment groups were sacrificed and removed at 14 days of different treatments.

The body weights of all groups exhibited a slight growth trend (Fig. 4d), indicating no significant systemic toxicity of the Te NSs based platform. To further evaluate *in vivo* biocompatibility in the histological level, the major organs of mice in each group were acquired in the endpoint and prepared for hematoxylin and eosin (H&E) staining. The H&E staining images (Fig. S6, Supporting Information) suggested no obvious inflammation or tissue damage in major organs in each group, which supports the excellent biocompatibility of Te NS-based nanomedicine.

4. Conclusions

In summary, a facile and versatile Te NSs-based nanoplatform for simultaneous cancer thermo-chemotherapy is presented. The drug carrier-Te NSs, are prepared through a liquid-phase exfoliation method and then modified by DSPE-PEG. The obtained Te-PEG NSs exhibited excellent biocompatibility, good stability, outstanding light-to-heat conversion efficiency under 808 nm laser irradiation (55%), and a considerable loading capacity of DOX (162%). Besides, Te-PEG/DOX NSs could also achieve pH- and NIR irradiation-triggered drug release in the acidic tumor microenvironment. Furthermore, the excellent thermo-chemotherapy results of Te-PEG/DOX NSs were confirmed *in vitro* and *in vivo* experiments. Therefore, the Te-PEG/DOX NSs with integrative thermo-chemotherapy properties can efficiently eliminate tumors effectively.

Declaration of competing interest

The authors declared that they have no conflicts of interest to this work. We declare that we do not have any commercial or associative interest that represents a conflict of interest in connection with the work submitted.

Acknowledgments

Financial support by the National Natural Science Foundation of China (No. 21871246), the Grant of Jilin Province Science & Technology Committee (No. 20200201082JC, 20180101194JC), Jilin Province Education Department the Science & Technology development project (No. JJKH20200741KJ, JJKH20200449KJ) are acknowledged.

Appendix A. Supplementary data

Supplementary data to this article can be found online at https://doi.org/10.1016/j.bioactmat.2021.11.010.

Author statement

WP: Writing - orignal draft, wrote the main draft under, All authors read and approved the final manuscript. CL: Writing - orignal draft, wrote the main draft under, All authors read and approved the final manuscript. YL: Writing - orignal draft, wrote the main draft, All authors read and approved the final manuscript. YY helped in paper writing, All authors read and approved the final manuscript. WL Writing - orignal draft, helped in final editing. All authors read and approved the final manuscript. CF: Supervision. Writing - orignal draft, All authors read and approved the final manuscript. LL: Writing - orignal draft, wrote the main draft, All authors read and approved the final manuscript.

References

[1] K.S. Novoselov, A.K. Geim, S.V. Morozov, D. Jiang, Y. Zhang, S.V. Dubonos, I. V. Grigorieva, A.A. Firsov, Electric field effect in atomically thin carbon films, Science 306 (2004) 666, https://doi.org/10.1021/acs.chemmater.8b00934.

[2] a) K. Hu, L. Xie, Y.D. Zhang, M. Hanyu, Z.M. Yang, K. Nagatsu, H. Suzuki, J. Ouyang, X.Y. Ji, J.J. Wei, H. Xu, O.C. Farokhzad, S.H. Liang, L. Wang, W. Tao, M. R. Zhang, Marriage of black phosphorus and Cu^{2+} as effective photothermal agents for PET-guided combination cancer therapy, Nat. Commun. 11 (1) (2020) 2778, https://doi.org/10.1038/s41467-020-16513-0;
b) W. Tao, N. Kong, X.Y. Ji, Y.P. Zhang, A. Sharma, J. Ouyang, B.W. Qi, J. Q. Wang, N. Xie, C. Kang, H. Zhang, O.C. Farokhzad, J.S. Kim, Emerging two-dimensional monoelemental materials (Xenes) for biomedical applications, Chem. Soc. Rev. 48 (11) (2019) 2891–2912, https://doi.org/10.1039/C8CS00823J;
c) C. Liu, H.S. Kim, M. Won, E. Jung, J.S. Kim, Navigating 2D monoelementalmaterials (Xenes) for cancer nanomedicine, Matter 3 (1) (2020) 12–13, https://doi.org/10.1016/j.matt.2020.06.004;
d) Z.M. Tang, N. Kong, J. Ouyang, C. Feng, N.Y. Kim, X.Y. Ji, C. Wang, O. C. Farokhzad, H. Zhang, W. Tao, Phosphorus science-oriented design and synthesis of multifunctional nanomaterials for biomedical applications, Matter 2 (2) (2020) 297–322, https://doi.org/10.1016/j.matt.2019.12.007;
e) C. Fang, J. Ouyang, Z.M. Tang, N. Kong, Y. Liu, L.Y. Fu, X.Y. Ji, T. Xie, O. C. Farokhzad, W. Tao, Germanene-based theranostic materials for surgical adjuvant treatment: inhibiting tumor recurrence and wound infection, Matter 3 (2020) 127, https://doi.org/10.1016/j.matt.2020.04.022.

[3] R. Paul, L. Zhu, H. Chen, J. Qu, L.M. Dai, Recent Advances in carbon-based metal-free electrocatalysts, Adv. Mater. 31 (31) (2019) 1806403, https://doi.org/10.1002/adma.201806403.

[4] Y.H. Jin, Y.M. Hu, W. Zhang, Tessellated multiporous two-dimensional covalent organic frameworks, Nat. Rev. Chem. 1 (7) (2017) 56, https://doi.org/10.1038/s41570-017-0056.

[5] K.W. Nam, S.S. Park, R. dos Reis, V.P. Dravid, H. Kim, C.A. Mirkin, J.F. Stoddart, Conductive 2D metal-organic framework for high-performance cathodes in aqueous rechargeable zinc batteries, Nat. Commun. (2019) 4948, https://doi.org/10.1038/s41467-019-12857-4.

[6] Y. Zhang, Y.Y. Yao, M.G. Sendeku, L. Yin, X.Y. Zhan, F. Wang, Z.X. Wang, J. He, Recent progress in CVD growth of 2D transition metal dichalcogenides and related heterostructures, Adv. Mater. 31 (41) (2019) 1901694, https://doi.org/10.1002/adma.201901694.

[7] Q.R. Cai, D. Scullion, W. Gan, A. Falin, S.Y. Zhang, K. Watanabe, T. Taniguchi, Y. Chen, E.J.G. Santos, L.H. Li, High thermal conductivity of high-quality monolayer boron nitride and its thermal expansion, Sci. Adv 5 (6) (2019), https://doi.org/10.1126/sciadv.aav0129 eaav0129.

[8] N.A. Jose, H.C. Zeng, A.A. Lapkin, Hydrodynamic assembly of two-dimensional layered double hydroxide nanostructures, Nat. Commun. 9 (2018) 4913, https://doi.org/10.1038/s41467-018-07395-4.

[9] a) X.Y. Ji, Y. Kang, J. Ouyang, Y.H. Chen, D. Artzi, X.B. Zeng, Y.L. Xiao, C. Feng, B. W. Qi, N.Y. Kim, P.E. Saw, N. Kong, O.C. Farokhzad, W. Tao, Synthesis of ultrathin biotite nanosheets as an intelligent theranosticplatform for combination cancer therapy, Adv. Sci. 6 (19) (2019) 1901211, https://doi.org/10.1002/advs.201901211;
b) C. Ouyang, X.Y. Feng, L. Ji, H.K. Li, N.Y. Gutti, D. Kim, A. Artzi, N. Xie, Y. N. Kong, G.J. Liu, X.B. Tearney, W. Sui, O.C. Tao, Farokhzad. 2D monoelemental germanene quantum dots: synthesis as robust photothermal agents for photonic cancer nanomedicine, Angew. Chem. Int. Ed 58 (38) (2019) 13405–13410, https://doi.org/10.1002/anie.201908377;
c) N. Kong, X.Y. Ji, J.Q. Wang, X.N. Sun, G.Q. Chen, T.J. Fan, W.Y. Liang, H. Zhang, A.Y. Xie, O.C. Farokhzad, W. Tao, ROS-mediated selective killing effect of black phosphorus: mechanistic understanding and its guidance for safe biomedical applications, Nano Lett 20 (5) (2020) 3943–3955, https://doi.org/10.1021/acs.nanolett.0c01098;
d) N. Kong, H.J. Zhang, C. Feng, C. Liu, Y.F. Xiao, X.C. Zhang, L. Mei, J.S. Kim, W. Tao, X.Y. Ji, Arsenene-mediated multiple independently targeted reactive oxygen species burst for cancer therapy, Nat. Commun. 12 (2021) 4777, https://doi.org/10.1038/s41467-021-24961-5;
e) C. Liu, S. Sun, Q. Feng, G.W. Wu, Y.T. Wu, N. Kong, Z.S. Yu, J.L. Yao, X. C. Zhang, W. Chen, Z.M. Tang, Y.F. Xiao, X.G. Huang, A. Lv, C.Y. Yao, H.B. Cheng, A.G. Wu, T. Xie, W. Tao, Arsenene nanodots with selective killing effects and their low-dose combination with ß-elemene for cancer therapy. Adv, Mater (2021) 2102054–2102068, https://doi.org/10.1002/adma.202102054.

[10] a) X.Y. ji, L.L. Ge, C. Liu, Z.M. Tang, Y.F. Xiao, W. Chen, Z.Y. Lei, W. Gao, S. Blake, D. De, B.Y. Shi, X.B. Zeng, N. Kong, X.C. Zhang, W. Tao, Capturing functional two-dimensional nanosheets from sandwich-structure vermiculite for cancer theranostics, Nat. Commun. 12 (2021) 1124, https://doi.org/10.1038/s41467-021-21436-5;
b) X.Y. Ji, Y. Kang, J. Ouyang, Y.H. Chen, D. Artzi, X.B. Zeng, Y.L. Xiao, C. Feng, B. W. Qi, N.Y. Kim, P.E. Saw, N. Kong, O.C. Farokhzad, W. Tao, Synthesis of ultrathin biotite nanosheets as an intelligent theranostic platform for combination cancer therapy, Adv. Sci. 6 (2019) 1901211–1901221, https://doi.org/10.1002/advs.201901211;
c) C. Pan, M.T. Ou, Q.Z. Cheng, Y. Zhou, Y.K. Yu, Z.M. Li, F. Zhang, D.H. Xia, M. Lin, X.Y. Ji, Z-scheme heterojunction functionalized pyrite nanosheets for modulating tumor microenvironment and strengthening photo/chemodynamic therapeutic effects, Adv. Funct. Mater. 30 (2020) 1906466–1906477, https://doi.org/10.1002/adfm.201906466;
d) M.T. Qu, C. Pan, Y.K. Yu, X. Wang, Y. Zhou, H.J. Zhang, Q.Z. Cheng, M.Y. Wu, X.Y. Ji, L. Mei, Two-dimensional highly oxidized ilmenite nanosheets equipped with Z-scheme heterojunction for regulating tumor microenvironment and enhancing reactive oxygen species generation, Chem. Eng. J. 390 (2020) 124524–124536, https://doi.org/10.1016/j.cej.2020.124524.

[11] a) H. Zhang, Ultrathin two-dimensional nanomaterials, ACS Nano 9 (10) (2015) 9451–9469, https://doi.org/10.1021/acsnano.5b05040;
b) S.Z. Butler, S.M. Hollen, L. Cao, Y. Cui, J.A. Gupta, H.R. Gutierrez, T.F. Heinz, S. S. Hong, J. Huang, A.F. Ismach, E. Johnston-Halperin, M. Kuno, V.V. Plashnitsa, R. D. Robinson, R.S. Ruoff, S. Salahuddin, J. Shan, L. Shi, M.G. Spencer, M. Terrones,

W. Windl, J.E. Goldberger, Progress, challenges, and opportunities in two-dimensional materials beyond graphene, ACS Nano 7 (4) (2013) 2898–2926, https://doi.org/10.1021/nn400280c.

[12] a) X. Kong, Q. Liu, C. Zhang, Z. Peng, Q. Chen, Elemental two-dimensional nanosheets beyond graphene, Chem. Soc. Rev. 46 (8) (2017) 2127–2157, https://doi.org/10.1039/c6cs00937a;
b) W. Tao, X.Y. Ji, X.D. Xu, M.A. Islam, Z.J. Li, S. Chen, P.E. Saw, H. Zhang, Z. Bharwani, Z.L. Guo, J.J. Shi, O.C. Farokhzad, Antimonene quantum dots: synthesis and application as near-infrared photothermal agents for effective cancer therapy, Angew. Chem. Int. Ed 56 (39) (2017) 11896–11900, https://doi.org/10.1002/anie.201703657.

[13] W. Tao, X. Ji, X. Zhu, L. Li, J. Wang, Y. Zhang, P.E. Saw, W. Li, N. Kong, M.A. Islam, T. Gan, X. Zeng, H. Zhang, M. Mahmoudi, G.J. Tearney, O.C. Farokhzad, Two-dimensional antimonene-based photonic nanomedicine for cancer theranostics, Adv. Mater. 30 (38) (2018) 1802061, https://doi.org/10.1002/adma.201802061.

[14] P.P. Lei, R. An, P. Zhang, S. Yao, S.Y. Song, L.L. Dong, X. Xu, K.M. Du, J. Feng, H. J. Zhang, Ultrafast synthesis of ultrasmall poly(vinylpyrrolidone)-protected bismuth nanodots as a multifunctional theranostic agent for in vivo dual-modal CT/photothermal-imaging-guided photothermal therapy, Adv. Funct. Mater. 27 (35) (2017) 1702018, https://doi.org/10.1002/adfm.201702018.

[15] X.T. Meng, X.H. Wang, Z.C. Cheng, N. Tian, M.C. Lang, W.J. Yan, D.M. Liu, Y. Z. Zhang, P. Wang, Photoluminescence lifetime of black phosphorus nanoparticles and their applications in live cell imaging, ACS Appl. Mater. Interfaces 10 (37) (2018) 31136–31145, https://doi.org/10.1021/acsami.8b11648.

[16] X. Ji, N. Kong, J. Wang, W. Li, Y. Xiao, S.T. Gan, Y. Zhang, Y. Li, X. Song, Q. Xiong, S. Shi, Z. Li, W. Tao, H. Zhang, L. Mei, J. Shi, A novel top-down synthesis of ultrathin 2D boron nanosheets for multimodal imaging-guided cancer therapy, Adv. Mater. 30 (36) (2018) e1803031, https://doi.org/10.1002/adma.201803031.

[17] Y. Lin, Y. Wu, R. Wang, G. Tao, P.F. Luo, X. Lin, G. Huang, J. Li, H.H. Yang, Two-dimensional Tellurium nanosheets for photoacoustic imaging-guided photodynamic therapy, Chem. Commun. 54 (62) (2018) 8579–8582, https://doi.org/10.1039/c8cc04653k.

[18] W. Tao, X. Zhu, X. Yu, X. Zeng, Q. Xiao, X. Zhang, X. Ji, X. Wang, J. Shi, H. Zhang, L. Mei, Black phosphorus nanosheets as a robust delivery platform for cancer theranostics, Adv. Mater. 29 (1) (2017) 1603276, https://doi.org/10.1002/adma.201603276.

[19] a) L.M. Wu, W.C. Huang, Y.Z. Wang, J.L. Zhao, D.T. Ma, Y.J. Xiang, L.Q. Li, J. S. Ponraj, S.C. Dhanabalan, H. Zhang, 2D tellurium based high-performance all-optical nonlinear photonic devices, Adv. Funct. Mater. 29 (4) (2019) 1806346. Doi: 10.1002\\adfm.201806346;
b) L. Tong, X.Y. Huang, P. Wang, L. Ye, M. Peng, L.C. An, Q.D. Sun, Y. Zhang, G. M. Yang, Z. Li, F. Zhong, F. Wang, Y.X. Wang, M. Motlag, W.Z. Wu, G.J. Cheng, W. D. Hu, Stable mid-infrared polarization imaging based on quasi-2D tellurium at room temperature, Nat. Commun. 11 (1) (2020) 2308, https://doi.org/10.1038/s41467-020-16125-8;
c) L. Shi, X.H. Ren, Q. Wang, Y.X. Li, F. Ichihara, H.W. Zhang, Y. Izumi, L. Ren, W. Zhou, Y. Yang, J.H. Ye, Stabilizing atomically dispersed catalytic sites on Tellurium nanosheets with strong metal-support interaction boosts photocatalysis, Small 16 (35) (2020) 2002356, https://doi.org/10.1002/smll.202002356.

[20] a) T. Yang, H. e, Q. Wang, Y. Tang, Y. Deng, H. Yang, X. Yang, P. Yang, D. Ling, C. Chen, Y. Zhao, H. Wu, H. Chen, Bifunctional tellurium nanodots for photo-induced synergistic cancer therapy, ACS Nano 11 (10) (2017) 10012–10024, https://doi.org/10.1021/acsnano.7b04230;
b) W. Huang, Y. Huang, Y. You, T. Nie, T. Chen, High-yield synthesis of multifunctional tellurium nanorods to achieve simultaneous chemo-photothermal combination cancer therapy, Adv. Funct. Mater. 27 (33) (2017) 1701388, https://doi.org/10.1002/adfm.201701388.

[21] a) N. Yu, J. Li, Z. Wang, S. Yang, Z. Liu, Y. Wang, M. Zhu, D. Wang, Z. Chen, Blue Te nanoneedles with strong NIR photothermal and laser-enhanced anticancer effects as "all-in-one" nanoagents for synergistic thermo-chemotherapy of tumors, Adv. Healthc. Mater. 7 (210) (2018), https://doi.org/10.1002/adhm.201800643 e1800643;
b) W. Huang, L. He, J. Ouyang, Q. Chen, C. Liu, W. Tao, T. Chen, Triangle-Shaped Tellurium nanostars potentiate radiotherapy by boosting checkpoint blockade immunotherapy, Matter 3 (5) (2020) 1725–1753, https://doi.org/10.1016/j.matt.2020.08.027.

[22] C. Gibaja, D. Rodriguez-San-Miguel, P. Ares, J. Gomez-Herrero, M. Varela, R. Gillen, J. Maultzsch, F. Hauke, A. Hirsch, G. Abellan, F. Zamora, Few-layer antimonene by liquid-phase exfoliation, Angew. Chem. Int. Ed. 55 (46) (2016) 14343–14347, https://doi.org/10.1002/anie.201605298.

[23] G. Kresse, J. Hafner, Ab initio molecular-dynamics simulation of the liquid-metal-amorphous-semiconductor transition in germanium, Phys. Rev. B 49 (20) (1994) 14251–14269, https://doi.org/10.1103/PhysRevB.49.14251.

[24] T. Liu, C. Wang, X. Gu, H. Gong, L. Cheng, X.Z. Shi, L.Z. Feng, B.Q. Sun, Z. Liu, Drug delivery with PEGylated MoS_2 nano-sheets for combined photothermal and chemotherapy of cancer, Adv. Mater. 26 (21) (2014) 3433–3440, https://doi.org/10.1002/adma.201305256.

[25] G. Liu, Z.B. Gao, J. Ren, Anisotropic thermal expansion and thermodynamic properties of monolayer β-Te, Phys. Rev. B 99 (19) (2019) 195436, https://doi.org/10.1103/PhysRevB.99.195436.

[26] S. Ghosh, T. Avellini, A. Petrelli, I. Kriegel, R. Gaspari, G. Almeida, G. Bertoni, A. Cavalli, F. Scotognella, T. Pellegrino, L. Manna, Colloidal $CuFeS_2$ nanocrystals: intermediate Fe d-band leads to high photothermal conversion efficiency, Chem. Mater. 28 (13) (2016) 4848–4858, https://doi.org/10.1021/acs.chemmater.6b02192.

[27] D.L. Meng, S.J. Yang, L. Guo, G.X. Li, J.C. Ge, Y. Huang, C. Bielawski, J.X. Geng, The enhanced photothermal effect of graphene/conjugated polymer composites: photoinduced energy transfer and applications in photocontrolled switches, Chem. Commun. 50 (92) (2014) 14345–14348, https://doi.org/10.1039/c4cc06849a.

[28] W. Feng, L. Chen, M. Qin, X.J. Zhou, Q.Q. Zhang, Y.K. Miao, K.X. Qiu, Y.Z. Zhang, C.L. He, Flower-like PEGylated MoS_2 nanoflakes for near-infrared photothermal cancer therapy, Sci. Rep. 5 (2015) 17422, https://doi.org/10.1038/srep17422.

[29] D. Chimene, D.L. Alge, A.K. Gaharwar, Two-dimensional nanomaterials for biomedical applications: emerging trends and future prospects, Adv. Mater. 27 (45) (2015) 7261–7284, https://doi.org/10.1002/adma.201502422.

[30] G. Yang, L. Xu, Y. Chao, J. Xu, X. Sun, Y. Wu, R. Peng, Z. Liu, Hollow MnO_2 as a tumor-microenvironment responsive biodegradable nano-platform for combination therapy favoring antitumor immune responses, Nat. Commun. 8 (2017) 902, https://doi.org/10.1038/s41467-017-01050-0.

[31] J.H. Park, G.V. Maltzahn, L.L. Ong, A. Centrone, T.A. Hatton, E. Ruoslahti, S. N. Bhatia, M.J. Sailor, Cooperative nanoparticles for tumor detection and photothermally triggered drug delivery, Adv. Mater. 22 (8) (2010) 880, https://doi.org/10.1002/adma.200902895.

[32] a) S. Chen, C. Xing, D. Huang, C. Zhou, B. Ding, Z. Guo, Z. Peng, D. Wang, X. Zhu, S. Liu, Z. Cai, J. Wu, J. Zhao, Z. Wu, Y. Zhang, C. Wei, Q. Yan, H. Wang, D. Fan, L. Liu, H. Zhang, Y. Cao, Eradication of tumor growth by delivering novel photothermal selenium-coated tellurium nanoheterojunctions, Sci. Adv 6 (15) (2020), https://doi.org/10.1126/sciadv.aay6825 eaay6825;
b) W. Huang, H. Wu, X. Li, T. Chen, Facile one-pot synthesis of tellurium nanorods as antioxidant and anticancer agents, Chem. Asian J. 11 (16) (2016) 2301–2311, https://doi.org/10.1002/asia.201600757;
c) L. Xu, H.W. Liang, H.H. Li, K. Wang, Y. Yang, L.T. Song, X. Wang, S.H. Yu, Understanding the stability and reactivity of ultrathin tellurium nanowires in solution: an emerging platform for chemical transformation and material design, Nano Res. 8 (4) (2014) 1081–1097, https://doi.org/10.1007/s12274-014-0586-9.

[33] J. Chen, X.Z. Qiu, J. Ouyang, J.M. Kong, W. Zhong, M. Xing, pH and reduction dual-sensitive copolymeric micelles for intracellular doxorubicin delivery, Biomacromolecules 12 (10) (2011) 3601–3611, https://doi.org/10.1021/bm200804j.